We are IntechOpen, the world's leading publisher of Open Access books Built by scientists, for scientists

6,900
Open access books available

185,000
International authors and editors

200M
Downloads

Our authors are among the

154
Countries delivered to

TOP 1%
most cited scientists

12.2%
Contributors from top 500 universities



WEB OF SCIENCE™

Selection of our books indexed in the Book Citation Index in Web of Science™ Core Collection (BKCI)

Interested in publishing with us?
Contact book.department@intechopen.com

Numbers displayed above are based on latest data collected.
For more information visit www.intechopen.com



Chapter 19

The Influence of Vanadium Doping on the Physical and Electrical Properties of Non-Volatile Random Access Memory Using the BTV, BLTV, and BNTV Oxide Thin Films

Kai-Huang Chen, Chien-Min Cheng, Sean Wu, Chin-Hsiung Liao and Jen-Hwan Tsai

Additional information is available at the end of the chapter

http://dx.doi.org/10.5772/52203

1. Introduction

Recently, the various functional thin films were widely focused on the applications in non-volatile random access memory (NvRAM), such as smart cards and portable electrical devices utilizing excellent memory characteristics, high storage capacity, long retention cycles, low electric consumption, non-volatility, and high speed readout. Additionally, the various non-volatile random access memory devices such as, ferroelectric random access memory (FeRAM), magnetron memory (MRAM), resistance random access memory (RRAM), and flash memory were widely discussed and investigated [1-9]. However, the high volatile pollution elements and high fabrication cost of the complex composition material were serious difficult problems for applications in integrated circuit semiconductor processing. For this reason, the simple binary metal oxide materials such as ZnO, Al_2O_3, TiO_2, and Ta_2O_5 were widely considered and investigated for the various functional electronic product applications in resistance random access memory devices [10-12].

The (ABO_3) pervoskite and bismuth layer structured ferroelectrics (BLSFs) were excellent candidate materials for ferroelectric random access memories (FeRAMs) such as in smart cards and portable electric devices utilizing their low electric consumption, nonvolatility, high speed readout. The ABO_3 structure materials for ferroelectric oxide exhibit high remnant polarization and low coercive filed. Such as $Pb(Zr,Ti)O_3$ (PZT), $Sr_2Bi_2Ta_2O_9$ (SBT), $SrTiO_3$ (ST), $Ba(Zr,Ti)O_3$ (BZ1T9), and $(Ba,Sr)TiO_3$ (BST) were widely studied and discussed

INTECH
open science | open minds

© 2013 Chen et al.; licensee InTech. This is an open access article distributed under the terms of the Creative Commons Attribution License (http://creativecommons.org/licenses/by/3.0), which permits unrestricted use, distribution, and reproduction in any medium, provided the original work is properly cited.

for large storage capacity FeRAM devices. The (Ba,Sr)TiO_3 and Ba(Ti,Zr)O_3 ferroelectric materials were also expected to substitute the PZT or SBT memory materials and improve the environmental pollution because of their low pollution problem [9-15]. In addition, the high dielectric constant and low leakage current density of zirconium and strontium-doped BaTiO_3 thin films were applied for the further application in the high density dynamic random access memory (DRAM) [16-20].

Bismuth titanate system based materials were an important role for FeRAMs applications. The bismuth titanate system were given in a general formula of bismuth layer structure ferroelectric, $(Bi_2O_2)^{2+}(A_{n-1}B_nO_{3n+1})^{2-}$ (A=Bi, B=Ti). The high leakage current, high dielectric loss and domain pinning of bismuth titanate system based materials were caused by defects, bismuth vacancies and oxygen vacancies. These defects and oxygen vacancies were attributed from the volatilization of Bi_2O_3 of bismuth contents at elevated temperature [21-23].

1.1. ABO_3 pervoskite structure material system

For ABO_3 pervoskite structure such as, $BaTiO_3$ and BZ1T9, the excellent electrical and ferroelectric properties were obtained and found. For SOP concept, the ferroelectric BZ1T9 thin film on ITO substrate were investigated and discussed. For crystallization and grain grow of ferroelectric thin films, the crystal orientation and preferred phase of different substrates were important factors for ferroelectric thin films of MIM structures.

The XRD patterns of BZ1T9 thin films with 40% oxygen concentration on Pt/Ti/SiO_2/Si substrates from our previous study were shown in Fig. 1 [24-25]. The (111) and (011) peaks of the BZ1T9 thin films on Pt/Ti/SiO_2/Si substrates were compared with those on ITO substrates. The strongest and sharpest peak was observed along the Pt(111) crystal plane. This suggests that the BZ1T9 films grew epitaxially with the Pt(111) bottom electrode. However, the (111) peaks of BZ1T9 thin films were not observed for (400) and (440) ITO substrates. Therefore, we determined that the crystallinity and deposition rate of BZ1T9 thin films on ITO substrates differed from those in these study [24-27].

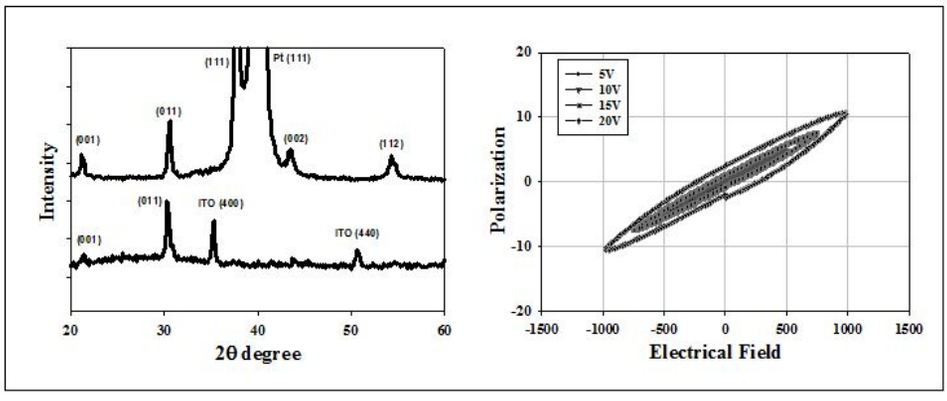


Figure 1. a) XRD patterns of as-deposited thin films on the ITO/glass and Pt substrates, and (b) *p-E* curves of thin films.

http://dx.doi.org/10.5772/52203

The polarization versus applied electrical field (*p-E*) curves of as-deposited BZ1T9 thin films were shown in Fig. 1(a). As the applied voltage increases, the remanent polarization of thin films increases from 0.5 to 2.5 μC/cm^2. In addition, the $2P_r$ and coercive field calculated and were about 5 μC/cm^2 and 250 kV/cm, respectively. According to our previous study, the BZ1T9 thin film deposited at high temperature exhibited high dielectric constant and high leakage current density because of its polycrystalline structure [24].

1.2. Bismuth Layer Ferroelectric Structure material system

The XRD patterns of as-deposited $Bi_4Ti_3O_{12}$ thin films and ferroelectric thin films under 500~700 °C rapid thermal annealing (RTA) process were compared in Fig. 2(a). From the results obtained, the (002) and (117) peaks of as-deposited $Bi_4Ti_3O_{12}$ thin film under the optimal sputtering parameters were found. The strong intensity of XRD peaks of $Bi_4Ti_3O_{12}$ thin film under the 700 °C RTA post-treatment were is found. They were (008), (006), (020) and (117) peaks, respectively. Compared the XRD patterns shown in Fig. 2, the crystalline intensity of (111) plane has no apparent increase as the as-deposited process is used and has apparent increase as the RTA-treated process was used. And a smaller full width at half maximum value (FWHM) is revealed in the RTA-treated $Bi_4Ti_3O_{12}$ thin films under the 700 °C post-treatment. This result suggests that crystal structure of $Bi_4Ti_3O_{12}$ thin films were improved in RTA-treated process.

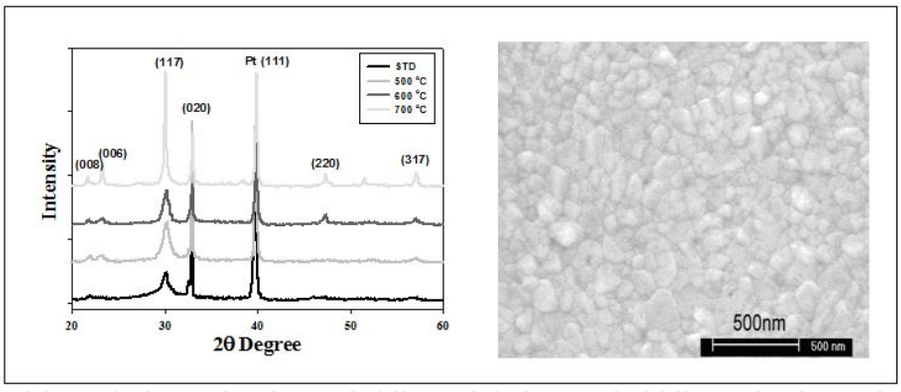


Figure 2. a) XRD patterns of as-deposited $Bi_4Ti_3O_{12}$ thin films, and (b)the SEM morphology of as-deposited $Bi_4Ti_3O_{12}$ films.

The surface morphology observations of as-deposited $Bi_4Ti_3O_{12}$ thin films under the 700 °C RTA processes were shown in Fig. 2(b). For the as-deposited $Bi_4Ti_3O_{12}$ thin films, the morphology reveals a smooth surface and the grain growth were not observed. The grain size and boundary of $Bi_4Ti_3O_{12}$ thin films increased while the annealing temperature increased to 700 °C. In RTA annealed $Bi_4Ti_3O_{12}$ thin films, the maximum grain size were about 200 nm and the average grain size is 100 nm. The thickness of annealed $Bi_4Ti_3O_{12}$ thin films were calculated and found from the SEM cross-section images. The thickness of the deposited $Bi_4Ti_3O_{12}$ thin films is about 800 nm and the deposited rate of $Bi_4Ti_3O_{12}$ thin films is about 14 nm/mim.

2. Experimental Detail

S. Y. Wu firstly reported that an MFS transistor fabricated by using bismuth titanate in 1974 [28-29]. The first ferroelectric memory device was fabricated by replacing the gate oxide of a conventional metal-oxide-semiconductor (MOS) transistor with a ferroelectric material. However, the interface and interaction problem between the silicon substrate and ferroelectric films were very important factors during the high temperature processes in 1TC structure. To overcome the interface and interaction problem, the silicon dioxide and silicon nitride films were used as the buffer layer. The low remnant polarization and high operation voltage of 1TC were also be induced by gate oxide structure with double-layer ferroelectric silicon dioxide thin films. Sugibuchi et al. provided a 50 nm silicon dioxide thin film between the $Bi_4Ti_3O_{12}$ layer and the silicon substrate [30].

The ferroelectric ceramic target prepared, the raw materials were mixed and fabricated by solid state reaction method. After mixing and ball-milling, the mixture was dried, grounded, and calcined for some time. Then, the pressed ferroelectric ceramic target with a diameter of two inches was sintered in ambient air. The base pressure of the deposited chamber was brought down 1×10^{-7} mTorr prior to deposition. The target was placed away from the $Pt/Ti/SiO_2/Si$ and SiO_2/Si substrate. For metal-ferroelectric-metal (MFM) capacitor structure, the Pt and the Ti were deposited by dc sputtering using pure argon plasma as bottom electrodes. The SiO_2 thin films were prepared by dry oxidation technology. The metal-ferroelectric-insulator-semiconductor (MFIS) and metal-ferroelectric-metal (MFM) structures were shown in Fig. 3.

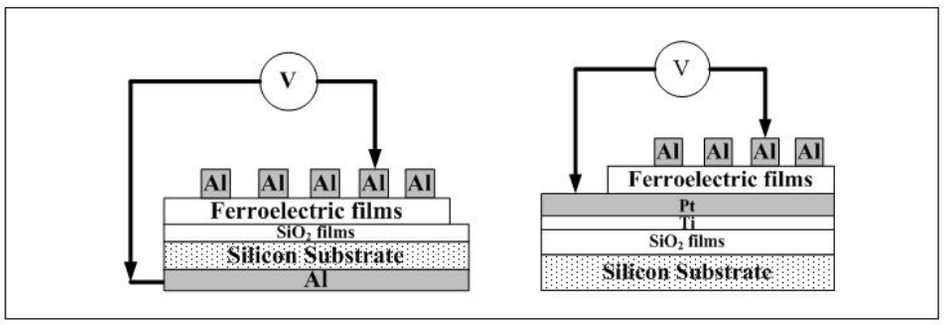


Figure 3. a) Metal-ferroelectric-insulator-semiconductor (MFIS) structure, and (b) Metal ferroelectric-metal (MFM) structure.

For the physical properties of ferroelectric thin films obtained, the thickness and surface morphology of ferroelectric thin films were observed by field effect scanning electron microscopy (FeSEM). The crystal structure of ferroelectric thin films were characterized by an X-ray diffraction (XRD) measurement using a Ni-filtered CuKα radiation. The capacitance-voltage (C-V) properties were measured as a function of applied voltage by using a Hewlett-Packard (HP 4284A) impedance gain phase analyzer. The current curves versus the applied voltage (I-V characteristics) of the ferroelectric thin films were measured by a Hewlett-Packard (HP 4156) semiconductor parameter analyzer.

http://dx.doi.org/10.5772/52203

3. Results and Discussion

3.1. Large memory window in the vanadium doped $Bi_4Ti_3O_{12}$ (BTV) thin films

The XRD pattern was used to identify the crystalline structures of as-deposited BTV thin films, labeled "vanadium doped at 550 °C," with various depositing parameters. From the XRD pattern, we found that the optimal deposition parameters of as-deposited BTV thin films were RF power of 130 W, chamber pressures of 10 mtorr and oxygen concentrations of 25%. The crystalline orientations of (117), (008) and (200) planes were apparently observed in the films. It was found that all of the films consisted of a single phase of a bismuth layered structure showing the preferred (008) and (117) orientation. Both films were well c-axis oriented, but BTV thin film was more c-axis oriented than BIT, labeled "undoped at 550 °C". For the polycrystalline BTV thin films, the (117) peak was the strongest peak and the intensity of the (008) peak was 10% of (117) peak intensity. An obvious change in the orientation due to the substitution was observed except for the degree of the (117) orientation for BTV films. In addition, the XRD patterns of the as-deposited BTV thin films deposited using optimal parameters at room and 550 °C substrate temperatures were observed in Fig. 2. This result indicated that the crystalline characteristics of BTV thin films deposited at 550 °C were better than those of BTV thin films at room temperature. The crystalline and dielectric characteristics of as-deposited BTV thin films were influenced by substrate temperatures. The electrical characteristics of as-deposited BTV thin films at substrate temperatures of 550 °C under optimal parameters will be further developed.

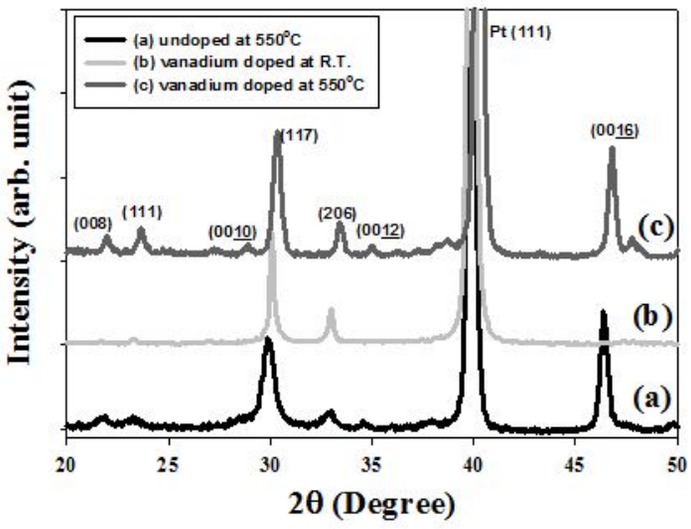


Figure 4. The XRD patterns of (a) undoped at 550 °C (b) vanadium doped at R.T. and (c) vanadium doped at 550 °C thin films deposited using optimal parameters.

In Fig. 5, circular-like grains with 150 nm width were observed with scanning electron microscopy (SEM) for as-deposited BTV thin films. From the cross-sectional SEM image, film thicknesses were measured to be 742 nm. As the depositing time increases from 30 and 60,

to 120 min, the thickness of as-deposited BTV thin films increases linearly from 197 and 386, to 742 nm, respectively, as the depositing rate decreases from 6.57 and 6.43, to 6.18 nm.

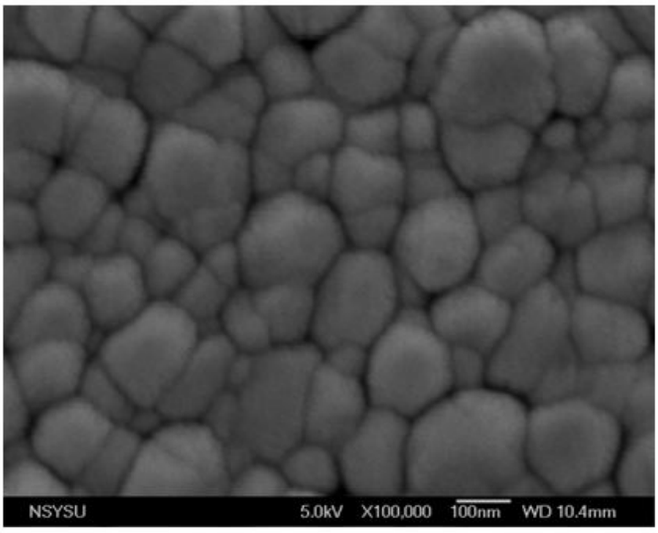


Figure 5. The surface micro structure morphology of the BTV thin films deposited using optimal parameters.

Figure 6(a) compares the change in the capacitance versus the applied voltage (*C-V*) for the un-doped and vanadium doped thin films. Based on Fig. 4, the capacitances of the BIT thin films appear to increase due to the vanadium dopant. We found that the capacitances of BTV thin films increased from 1.3 to 4.5 nF. As suggested by Fig. 4, the improvement in the dielectric constants of the BTV thin films can be attributed to the compensation of the oxygen vacancy and the improvement in the B-site substitution of the ABO_3 phase in the BTV thin films [31-34].

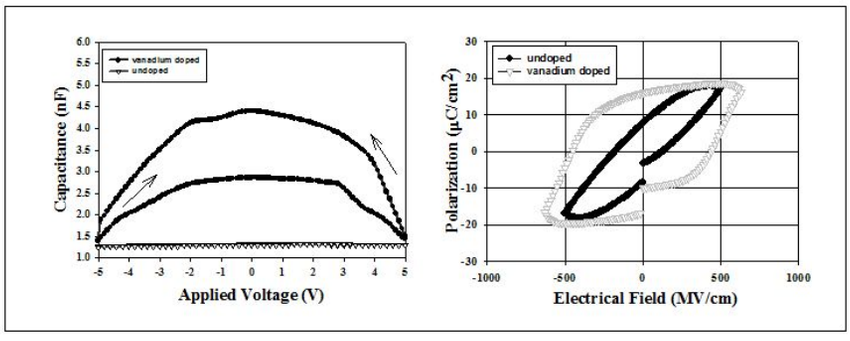


Figure 6. a) The P-E characteristics of vanadium doped and undoped thin films, and (b) The normalization C-V curves of vanadium doped and undoped thin films.

Figure 6 shows ferroelectric hysteresis loops of BIT and as-deposited BTV thin film capacitors measured with a ferroelectric tester (Radiant Technologies RT66A). The as-deposited BTV thin films, labeled "vanadium doped," clearly show ferroelectricity. The remanent po-

larization and coercive field were 23 μC/cm^2 and 450 kV/cm. Comparing the vanadium doped and undoped BIT thin films, the remanent polarization (2Pr) would be increased form 16μC/cm^2 for undoped BIT thin films to 23 μC/cm^2 for vanadium doped. However, the coercive field of as-deposited BTV thin films would be increased to 450 kV/cm. These results indicated that the substitution of vanadium was effective for the appearance of ferroelectricity at 550 °C. The 2Pr value and the Ec value were larger than those reported in Refs. [35-36], and the 2Pr value was smaller and the Ec value was larger than those reported in [37]. Based on above results, it was found that the simultaneous substitutions for B-site are effective to derive enough ferroelectricity by accelerating the domain nucleation and pinning relaxation caused by B-site substitution [31-37].

The leakage current density versus applied voltage curves of as-deposited BTV thin films for different depositing time on the MFIS structure were be found. We found that the leakage current density of undoped BIT thin films, labeled "undoped," were larger than those of vanadium-doped BIT thin films. This result indicated that the substitution of B-site in ABO_3 perovskite structure for BTV thin films was effective in lowering leakage current density. Besides, the thickness of BTV thin films has an apparent influence on the leakage current density of BTV thin films, and that will have an apparent influence on the other electrical characteristics of BTV thin films. At an electric field of 0.5 MV/cm, the leakage current density critically decreases from the 3.0 ×10^{-7} A/cm2 for 30 min-deposited BTV thin films to around 3×10^{-8}A/cm^2 and 2×10^{-8} A/cm^2 for 60 and 120 min-deposited BTV thin films.

Figure 7(a) show the capacitance versus applied voltage (*C-V*) curves of as-deposited vanadium doped BTV and un-doped BIT thin films. The applied voltages, which are first changed from -20 to 20 V and then returned to -20 V, are used to measure the capacitance voltage characteristics (*C-V*) of the MFIS structures. For the vanadium doped thin films, the memory window of MFIS structure increased from 5 to 15 V, and the threshold voltage decreased from 7 to 3 V. This result demonstrated that the lower threshold voltage and decreased oxygen vacancy in undoped BIT thin films had been improved from the *C-V* curves measured.

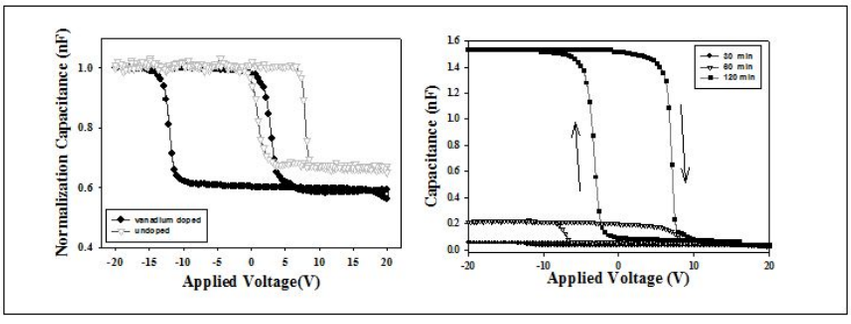


Figure 7. a) The P-E characteristics of vanadium doped and undoped thin films, and (b) The normalization *C-V* curves of vanadium doped and undoped thin films.

Figure 7(b) shows the *C-V* curves of 30 min-deposited BTV thin films, and Figure 7(b) compares the *C-V* curves of BTV thin films deposited at different depositing time. Figure 7(b) also shows that the capacitance at the applied voltage value of 0 V critically increases as the

depositing time increases. The memory window would be decreased from 15.1 and 13.4, to 10.6 V as the depositing time increased. Two reasons may be the cause that the increases capacitance of as-deposited BTV thin films in the MFIS structure for the different depositing time. First, the decrease leakage current density was attributed to the increase thickness of as-deposited BTV thin films in Fig. 4. Second, the different thickness and high dielectric constant of as-deposited BTV thin films are also an important factor. In Fig. 7, the capacitance of as-deposited BTV thin films for MFIS structure could be calculated from Eq. 1 and Eq. 2:

$$C = \varepsilon_0 \varepsilon_r \frac{A}{d} \tag{1}$$

$$\varepsilon_r = \frac{(\varepsilon_1 d_2 + \varepsilon_2 d_1)}{(d_1 + d_2)} \tag{2}$$

The ε1 and d1 are the effective dielectric constant and the total thickness of silicon and SiO_2 layer. The ε2 and d2 are the effective dielectric constant and the thickness of as-deposited BTV thin film layer. The relative dielectric constants of Si and SiO_2 are 11.7 and 3.9. The εr value (ε1) of silicon and SiO_2 layer is much smaller than that (ε2) of as-deposited BTV thin films. The ε1×d2 is the unchanged value and the ε2×d1 value increases with the increase of depositing time. In Eq. (2), the ε1×d2 increases more quickly as d2 increases. In Eq. (1), the C value will increase as the εr value increases.

For memory window characteristics at applied voltage of 0 volts, the upper and lower capacitance values of as-deposited BTV thin films for 30 min depositing time were 0.056 and 0.033 nF, respectively. For 60 min and 120 min depositing time, they were 0.215~0.048 nF and 1.515 ~0.105 nF, respectively. The change ratios at zero voltage were defined in Eq.(3) from these experimental results:

$$ratio = \frac{(C_u - C_l)}{C_u} \tag{3}$$

where Cu and Cl are the upper and lower capacitance values.

The capacitance change ratios of as-deposited BTV thin films for different depositing time were 41, 73 and 93%, respectively. From above statements, the good switching characteristics of ferroelectric polarization could be attributed to memory windows ratio and the thinner thickness of as-deposited BTV thin film for the depositing time of 30 min. These results indicted the upper and lower capacitance of memory window would be decreased by lowering the thickness of SiO_2 layer.

http://dx.doi.org/10.5772/52203

3.2. The Influence of Lanthanum Doping on the Physical and Electrical Properties of BTV (BLTV) Ferroelectric Thin Films

For MFM structures, the crystal orientation and preferred phase of ferroelectric thin films on $Pt/Ti/SiO_2/Si$ substrates was important factor. The x-ray diffraction (XRD) patterns of BLTV and BTV thin films prepared by rf magnetron sputtering were be found. From the XRD pattern, the BLTV and BTV thin film were polycrystalline structure. The (004), (006), (008), and (117) peaks were observed in the XRD pattern. All of thin films consisted of a single phase of a bismuth layered structure showing the preferred (117) orientation. All of thin films were exhibited well c axis orientation. The change in the orientation of BLTV thin films due to the substitution was not observed. The degree of the (117) orientation relative to the (001) orientation of BLTV thin films dominant was shown.

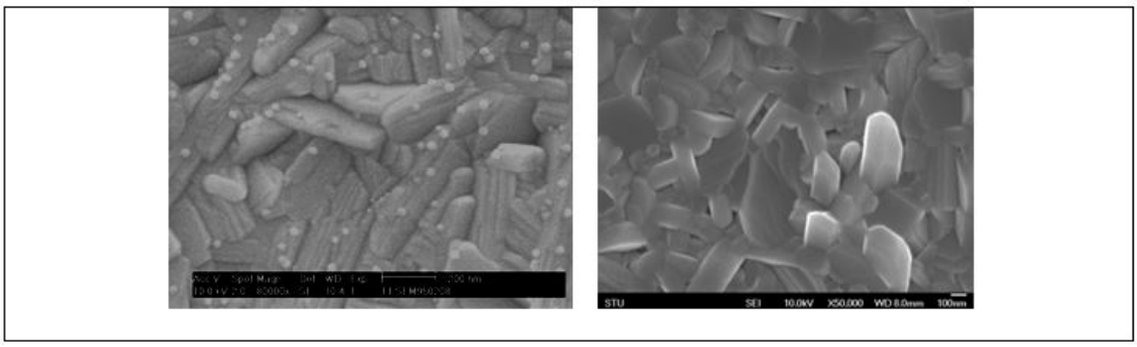


Figure 8. The surface micro structure of as-deposited (a) BTV and (b) BLTV thin films.

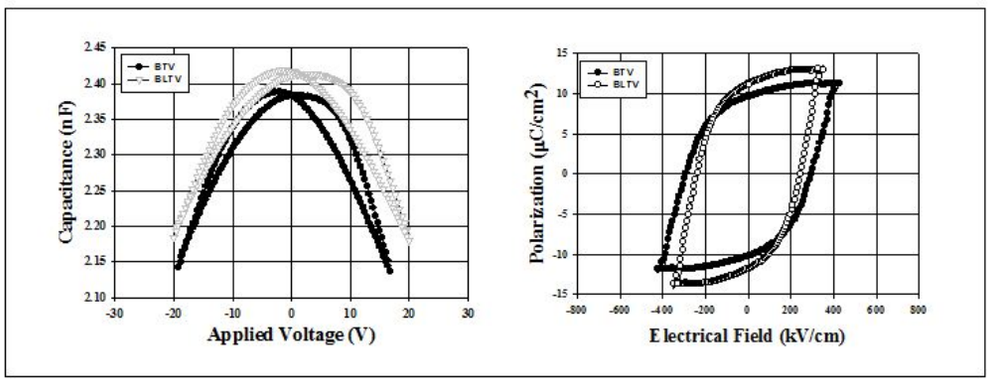


Figure 9. a)The *C-V* characteristics of as-deposited BTV and BLTV thin films. (b) The polarization versus electrical field characteristics of as-deposited BTV and BLTV thin films.

In Fig. 8a, rod-like and circular-board grains with 250 nm length and 150 nm width were observed with scanning electron microscopy (SEM) for as-deposited BTV films. The small grain was gold element in preparation for the SEM sample. However, the BLTV thin films exhibited a great quantity of 400 nm length and 100 nm width rod-like grain structure in Fig 8 b. The rod-like grain size of BLTV thin films was larger than those of BTV. We induced

that the bismuth vacancies of BTV thin films compensate for lanthanum addition and microstructure were improved in BLTV thin films. From the cross-sectional SEM image, average thin film thicknesses for MFIS structure were about 610 nm. The average thickness of thin films for MFM structure was about 672 nm.

Figure 9(a) shows the change in the capacitance versus the applied voltage (*C-V*) of the BTV and BLTV thin films in MFM structure measured at 100 kHz. The applied voltages, which were first changed from -20 to 20 V and then returned to -20 V, were used to measure the capacitance voltage characteristics (CV). The BLTV thin films exhibited high capacitance than those of BTV thin films. We found that the capacitances of the lanthanum-doped BTV thin films were increased from 2.38 to 2.42 nF.

Figure 9(b) shows the *p-E* curves of the different ferroelectric thin films under applied voltage of 18V from the Sawyer–Tower circuits. The remanent polarization of non-doped, vanadium-doped, and lanthanum-doped ferroelectric thin films linearly was increased from 5, 10 to 11 μC/cm^2, respectively. The coercive filed of non-doped, vanadium-doped, and lanthanum-doped ferroelectric thin films were about 300, 300, and 250 kV/cm, respectively. The ferroelectric properties of lanthanum-doped and vanadium-doped BIT thin films were improved and found.

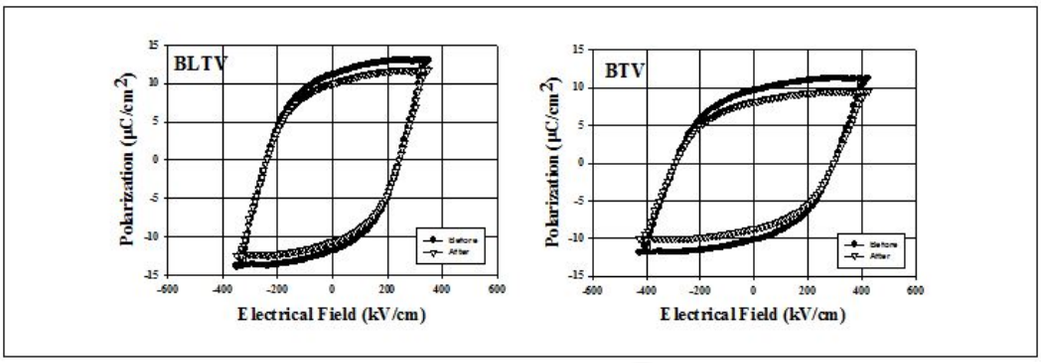


Figure 10. a)The *C-V* characteristics of as-deposited BTV and BLTV thin films. (b) The polarization versus electrical field characteristics of as-deposited BTV and BLTV thin films.

The fatigue characteristics for ferroelectric thin films were the time dependent change of the polarization state. After a long time, the polarization loss of ferroelectric thin films was affected by oxygen vacancies, defect, and space charge in the memory device. Figure 10 shows the polarization versus electrical field (*p-E*) properties of the different ferroelectric thin films before and after the switching of 10^9 cycles. The remnant polarization loss of BLTV and BTV thin films were about 9% and 15% of initial polarization value, respectively. The remnant polarization of BLTV thin films were little changed after the switching cycles. The fatigue behavior and domain pinning were improved by lanthanum and vanadium addition in BIT thin films. To reduce bismuth defect and oxygen vacancy, the high-valence cation substituted for the A-site of BLTV thin films were observed.

http://dx.doi.org/10.5772/52203

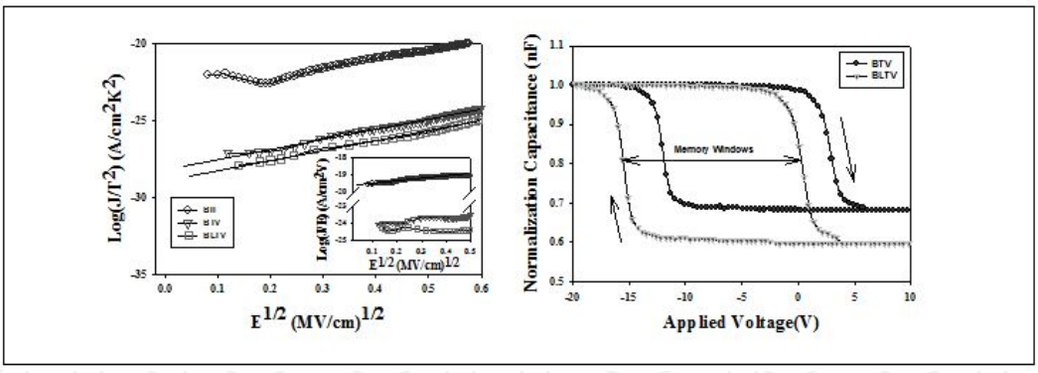


Figure 11. a) The (J/T^2) and (J/E) versus $E^{1/2}$ curves of as-deposited BIT, BTV, and BLTV thin films. (b) The normalization capacitance versus applied voltage curves of as-deposited BTV and BLTV thin films.

From the *J-E* curves, the conduction mechanism of as-deposited thin films was also proved the bismuth defect and oxygen vacancy results. For MFIS structure, the interface and interaction problem between of the silicon and ferroelectric films was serious important. The effect of the bound polarization charge from the carrier in the silicon substrate was observed. To overcome this problem, the insulator films of buffer layer were used for MFIS structure [28-30, 37-38].

Figure 11(a) shows the leakage current density versus electrical field (*J-E*) characteristics of as-deposited BTV and BLTV thin films for MFIS structure. The leakage current density of the as-deposited BLTV thin films were about one order of magnitude lower than those of the non-doped lanthanum thin films. However, the lanthanum and vanadium doped BIT thin films were lower than those of BIT thin films. We suggested that low leakage current density attributed to substituting a bismuth ion with a lanthanum ion at A-site for lanthanum doped BTV thin films. To discuss bismuth ion substituting by lanthanum ion effect, the leakage current versus electrical field curves of BLTV thin films were fitted to Schottky emission and Poole–Frankel transport models. The inset of Fig. 11(a) shows the JE characteristics for BIT, BTV, and BLTV thin films in terms of J/E as vertical axis and $E^{1/2}$ as horizontal axis. The fitting curves were straight in this figure and a JE curve of thin films was the Poole–Frankel emission model. The high leakage current was attributed to the bismuth vacancies and oxygen vacancies of as-deposited BIT thin films [39–42]. Park et al. also suggested that the enhanced stability of TiO_6 octahedra against oxygen vacancies for fatigue resistance of lanthanum doped BIT thin films [31].

In a previous study, the low threshold voltage of ferroelectric thin films was attributed by bismuth and oxygen vacancy [9]. The threshold voltage for the lanthanum-doped BTV thin films of MFIS structure was improved from 5 to 3 V. The memory functional effect and depletion delay of the MFIS structure was caused by remanent polarization of ferroelectric thin films in CV curves. In this study, the memory window was increased from 15 to 18 V. The large memory window of lanthanum-doped BTV thin films was also proved by *p-E* curves in Fig. 11(b). As a result, the improvement in the capacitance of the BLTV thin films was attributed to the compensation of the oxygen vacancy of the BLSF structure. Additionally, the

memory window of ferroelectric thin films was changed by the sweeping speed. The ferroelectric capacitance and threshold voltage of MFIS structure slightly decreases as the sweeping speed increases. That was influenced by the mobile ions and charge injection between as-deposited ferroelectric thin films and metal electrode as the sweeping speed increased [9].

3.3. The Influence of Neodymium Doping on the Physical and Electrical Properties of BTV (BNTV) Ferroelectric Thin Films

Figure 12(a) shows x-ray diffraction patterns of the as-deposited ferroelectric thin films for different oxygen concentration on ITO substrate. From the XRD patterns, we found that the ferroelectric thin films exhibited polycrystalline structure. In addition, the (117), (008), and (220) peaks were observed in the XRD pattern. The intensity of the (117) peak of the ferroelectric thin films increases linearly as the oxygen concentration increases from 0 to 40%. The intensity of the (117) peak of the as-deposited ferroelectric thin films decreases at oxygen concentration from 40 to 60%. As shown in Fig. 3, the (117) preferred phase and smallest full-width-half-magnitude (FWHM) value were exhibited by the as-deposited ferroelectric thin film with the 40% oxygen concentration. The polycrystalline structure of the as-deposited $(Bi_{3.25}Nd_{0.75})(Ti_{2.9}V_{0.1})O_{12}$ ferroelectric thin film was optimal at 40% oxygen concentration.

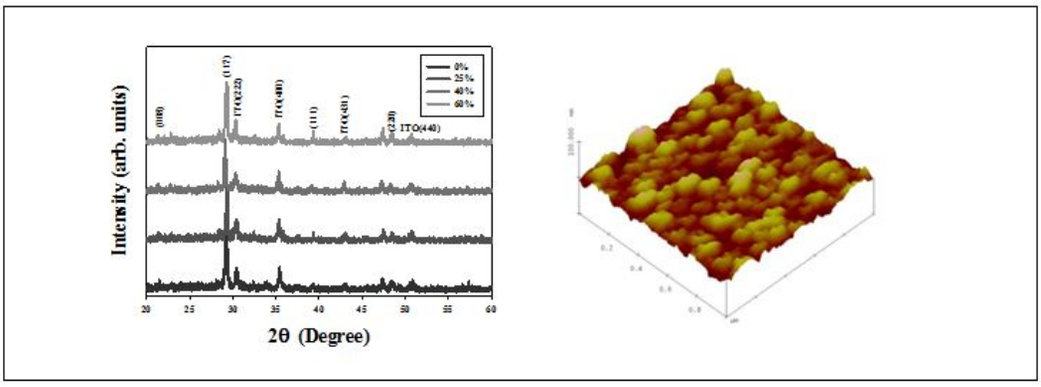


Figure 12. a) The x-ray diffraction patterns of the as-deposited $(Bi_{3.25}Nd_{0.75})(Ti_{2.9}V_{0.1})O_{12}$ ferroelectric thin film for the different oxygen concentration. (b) The surface morphology of the as-deposited $(Bi_{3.25}Nd_{0.75})(Ti_{2.9}V_{0.1})O_{12}$ ferroelectric thin film for 40% oxygen concentration.

Besides, the interface between an electrode and the as-deposited $(Bi_{3.25}Nd_{0.75})(Ti_{2.9}V_{0.1})O_{12}$ thin films was an important factor that seriously influences the physical and electrical properties of the MIM capacitor structure. Therefore, the surface roughness of the as-deposited $(Bi_{3.25}Nd_{0.75})(Ti_{2.9}V_{0.1})O_{12}$ thin films for 40% oxygen concentration was absolutely determined and calculated. Figure 12(b) shows the surface roughness of the as-deposited $(Bi_{3.25}Nd_{0.75})(Ti_{2.9}V_{0.1})O_{12}$ ferroelectric thin film from the AFM images. The roughness of the ferroelectric thin film were 4.278nm. The surface roughness of the as-deposited ferroelectric thin films increases with the oxygen concentration. Therefore, we assume that the surface roughness of the as-deposited ferroelectric thin films increases due to an increase in the crystallinity with oxygen concentration.

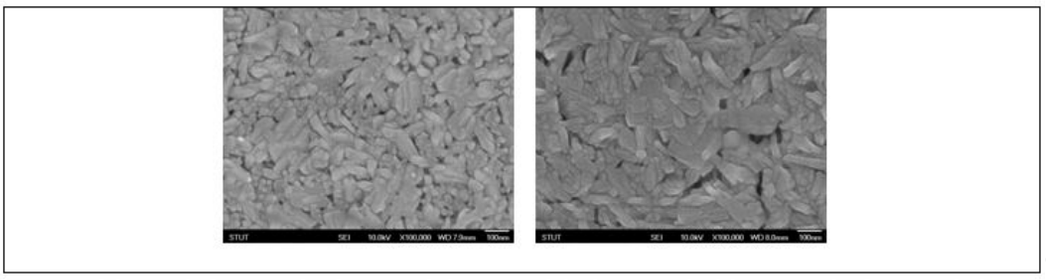


Figure 13. The surface morphology of the as-deposited $(Bi_{3.25}Nd_{0.75})(Ti_{2.9}V_{0.1})O_{12}$ ferroelectric thin film for 40% oxygen concentration. The surface micro-structure of the as-deposited $(Bi_{3.25}Nd_{0.75})(Ti_{2.9}V_{0.1})O_{12}$ ferroelectric thin film for (a) 25% and (b) 40% oxygen concentration.

From the SEM images in Fig. 13, the surface morphology and grain size of the as-deposited $(Bi_{3.25}Nd_{0.75})(Ti_{2.9}V_{0.1})O_{12}$ thin films for 25 and 40% oxygen concentration were observed. The grain size of the as-deposited $(Bi_{3.25}Nd_{0.75})(Ti_{2.9}V_{0.1})O_{12}$ thin films were about 110 nm and 50 nm, respectively. We deduced that grain size changed caused by the different oxygen xoncentration.

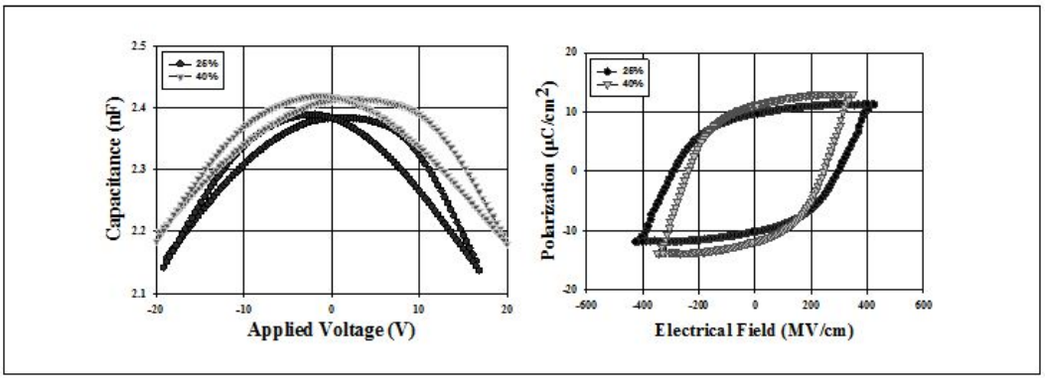


Figure 14. a) The capacitance versus applied voltage (C-V) properties of the as-deposited $(Bi_{3.25}Nd_{0.75})(Ti_{2.9}V_{0.1})O_{12}$ ferroelectric thin film. (b) The polarization versus applied electrical field (p-E) properties of the as-deposited $(Bi_{3.25}Nd_{0.75})(Ti_{2.9}V_{0.1})O_{12}$ ferroelectric thin film.

Figure 14(a) shows the *C-V* characteristics measured with the MFM capacitor structure for the as-deposited $(Bi_{3.25}Nd_{0.75})(Ti_{2.9}V_{0.1})O_{12}$ thin films deposited under various oxygen concentrations. The applied bias voltage is adjusted from -20 to 20V. The capacitance of ferroelectric thin films first increases with the increase of oxygen concentration and reaches the maximum value in the 40 % oxygen atmosphere. Then the capacitance apparently decreases in the further increase of oxygen to 60 %. This variation of capacitance has the similar results with the XRD patterns and the AFM images. The polarization versus applied electrical field (*p-E*) curves of the as-deposited $(Bi_{3.25}Nd_{0.75})(Ti_{2.9}V_{0.1})O_{12}$ ferroelectric thin film at the frequency of 1kHz were shown in fig. 14(b). From the *p-E* curves results, the remnant polarization of ferroelectric thin films were 11 $\mu C/cm^2$, as the coercive filed of 220 kV/cm. In addition, the remnant polarization and coercive filed of ferroelectric thin films for 40% oxygen concentration were about 10 $\mu C/cm^2$ and 300 kV/cm. From the experimental measurement, this result

was attributed to the suitable oxygen concentration sample as compared to that of the as-deposited ferroelectric thin film. As the oxygen/argon mixtures were used as the depositing atmosphere, the defects and oxygen vacancies in ferroelectric thin films were filled and compensated by oxygen gas, and the leakage current density were decreased. The low leakage current density will reveal in the 40%-oxygen-deposited ferroelectric thin films. For that the capacitance will be increased and the leakage current density will be decreased. As the applied voltage of 15V was used, the leakage current density of ferroelectric thin films deposited at 40% oxygen concentration is about 1×10^{-9}A/cm^2.

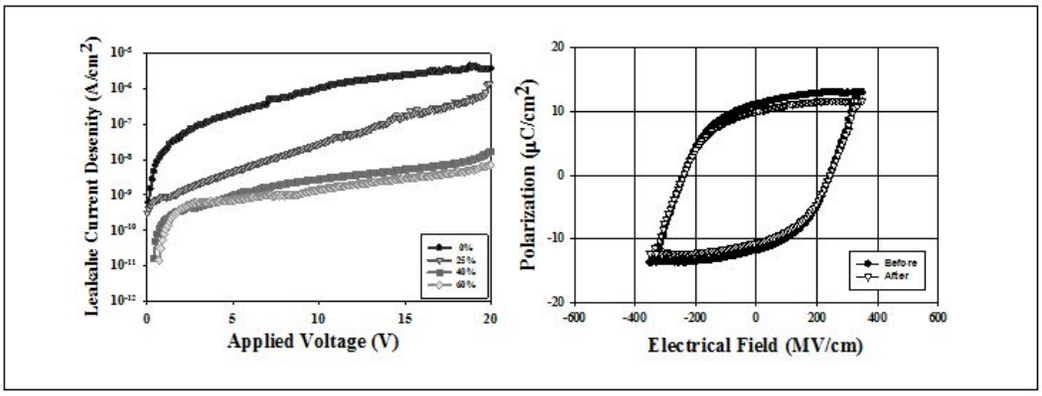


Figure 15. a) The leakage current density versus applied voltage (J-E) properties of the as-deposited $(Bi_{3.25}Nd_{0.75})(Ti_{2.9}V_{0.1})O_{12}$ ferroelectric thin film.(b) The retention and fatigue properties of the as-deposited ferroelectric thin film corresponding hysteresis loop before and after fatigue test.

The retention and fatigue properties for the as-deposited $(Bi_{3.25}Nd_{0.75})(Ti_{2.9}V_{0.1})O_{12}$ ferroelectric thin films were the time dependent change of the polarization state. After long time testing, the polarization loss of the as-deposited ferroelectric thin films was affected by oxygen vacancies, defect, and space charges in the memory device test. Figure 15 shows the polarization versus electrical field (*p-E*) properties of the as-deposited $(Bi_{3.25}Nd_{0.75})(Ti_{2.9}V_{0.1})O_{12}$ ferroelectric thin films before and after the switching of 10^9 cycles. The remnant polarization loss of ferroelectric thin films was about 9% of initial polarization value, respectively. The remnant polarization of ferroelectric thin films was little changed after the test cycles. The fatigue behavior and domain pinning were improved by neodymium and vanadium addition in BIT thin films. To improve bismuth and oxygen vacancy, the high-valence cation substituted for the A-site of $(Bi_{3.25}Nd_{0.75})(Ti_{2.9}V_{0.1})O_{12}$ thin films were observed.

3.4. Bipolar Resistive Switching Properties of Transparent Vanadium Oxide (V_2O_5) Resistive Random Access Memory

Figure 16(b) shows x-ray diffraction patterns of the as-deposited vanadium oxide thin films for 60% oxygen concentration on ITO substrate prepared by different sintering temperature. From the XRD patterns, we found that the vanadium oxide thin films exhibited polycrystalline structure. In addition, the (110), (222), and (400) peaks were observed in the XRD pattern. The intensity of the (110) peak of the thin films increases linearly as the sintering

temperature increases from 400 to 550 °C. The intensity of the (110) peak of the as-deposited thin films decreases at sintering temperature from 550 to 600 °C. As shown in Fig. 16, the (110) preferred phase and smallest full-width-half-magnitude (FWHM) value were exhibited by the as-deposited vanadium oxide thin film with the sintering temperature of 550 °C. The polycrystalline structure of the as-deposited vanadium oxide thin film was optimal at 550 °C sintering temperature.

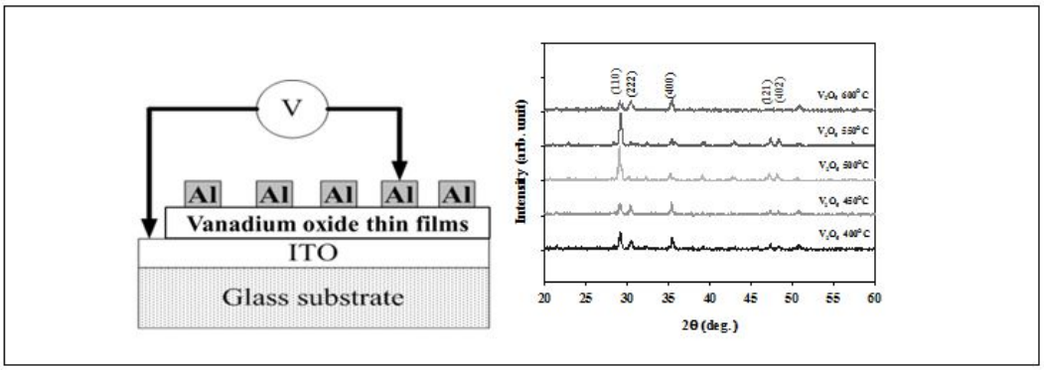


Figure 16. a) Metal-insulator-metal (MIM) structure using as-deposited vanadium oxide thin films. (b) The x-ray diffraction patterns of the as-deposited vanadium oxide thin films on ITO substrate for different sintering temperature.

The thickness of as-depoisted vandium oxide thin films for different sintering temperature was determined by SEM morphology. As the oxygen concentration increases from 0 to 60%, the thickness of as-deposited vandium oxide thin films linearly decreases. In addition, the deposition rate of as-deposited vanadium oxide thin films with 60% oxygen concentration was 2.62 nm/min. The decreases in the deposition rate and thickness of as-depoisted vanadium oxide thin films might be affected by the decrease in Ar/O_2 ratio. The Ar/O_2 ratio was adjusted using argon gas to generate the plasma on the surface of the as-depoisted vanadium oxide ceramic target during sputtering. Figure 17 shows the surface morphology for the as-deposited and 500 °C sintered vanadium oxide thin films. We found that the grain size of 500 °C sintered vanadium oxide thin films were larger than others. The better resistance properties might be caused by this reason.

Figure 18 shows the current vsersus applied voltage (*I-V*) properties of vanadium oxide thin films for the different sintering temperature. After the staring forming process, the device reached a low resistance state (LRS) and high resistance state (HRS). By sweeping the bias to negative over the reset voltage, a gradual decrease of current was presented to switch the cells from LRS to HRS (reset process). Additionally, the cell turns back to LRS while applying a larger positive bias than the set voltage (set process). All of the vanadium oxide thin film were exhibit the bipolar behavior. The *I-V* properties of as-deposited vanadium oxide thin films of 60% oxygen concentration was about $1\times10^{-4}A/cm^2$ when an applied electrical voltage of 0.1V. During the rf sputtering deposition process, oxygen vacancies appear in the as-deposited vanadium oxide thin films. The defects and oxygen vacancies of as-deposited vanadium oxide thin films were filled and compensated for to different extents at different oxygen concentrations. In addition, the smallest leakage current density of as-deposited vanadium oxide thin films

was obtained at an oxygen concentration of 40%. As shown in Fig. 18, the high leakage current density and thin films of as-deposited vanadium oxide thin films for 60% oxygen concentration were attributed to low argon sputtering gas concentration.

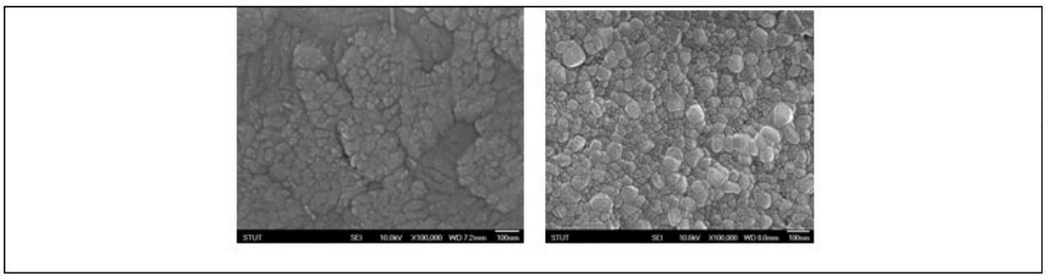


Figure 17. The surface morphology for (a) as-deposited (b) 500°C sintered vanadium oxide thin films.

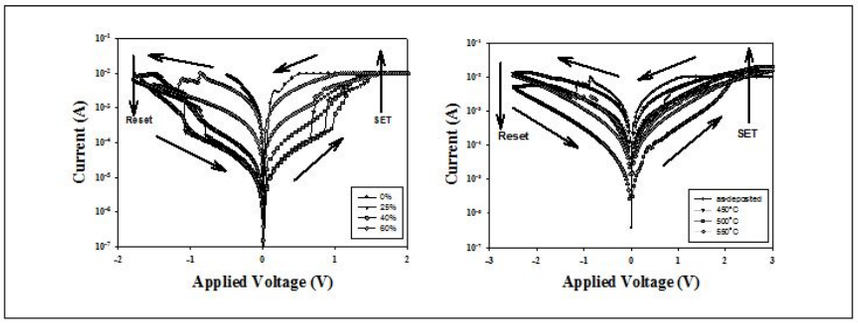


Figure 18. a) Typical *I-V* characteristics of vanadium oxide thin films for the different oxygen concentration. (b) Typical *I-V* characteristics of the as-deposited vanadium oxide thin films for different sintering temperature.

In addition, The transport current of the vanadium oxide thin films decreases linearly as the sintering temperature increases from 450 to 500 °C. The transport current of the as-deposited vanadium oxide thin films increases at sintering temperature from 500 to 550 °C. We found the as-deposited vanadium oxide thin films prepared by 500 °C sintering temperature were exhibited the large the on/off ratio resistance properties. In addition, the switching cycling was measured another type of reliability and retention characteristics were observed. There was a slight flucation of resistance in the HRS and LRS states, and the stable bipolar witching property was observed during 20 cycles. The results show remarkable reliability performance of the resistance random access memory devices for nonvolatile memory applications.

4. Conclusion

In conclusion, BIT, BTV, BNTV, and BLTV thin films were prepared by rf magnetron sputtering. We confirmed that all thin films on Pt/Ti/SiO_2/Si substrate well crystallized by XRD

analysis. The BNTV, BLTV, and BTV shows clear ferroelectricity form the *p-E* curves. The remnant polarization properties of BLTV thin film decreased by 9%, while that of the BTV decreased by 15% after the fatigue test with 10^9 switching cycles. Fatigue behavior in ferroelectric capacitors was attributed to oxygen and bismuth vacancies. The leakage current density of as-deposited BLTV and BTV thin films were lower than those of BIT, which were were attributed to the decrease of oxygen and ismuth vacancies after vanadium and lanthanum addition. The conduction mechanism of as-deposited BTV and BLTV thin films were also proved these results in *J-E* curves. We indicated that small ions substitution for A and B site of BLSF structure was effective decreased the oxygen and bismuth vacancies. Finally, the low threshold voltage and memory window of BLTV thin films were improved from the *C-V* curves measured. In addition, the metal oxide thin films such as, TiO_2, Ta_2O_5, Al_2O_3, and CuO were widely investigated and discussed for applications in nonvolatile resistive random access memory (RRAM) devices. The nonvolatile resistive random access memory (RRAM) devices were well developed and studied because of their structural simplicity, high density and low power, read / write speed (about 10^1 ~ 10^3ns), high operating cycles (> 10^{13}) and other non-volatile advantages. Therefore, the electrical switching properties of the vanadium oxide thin films for nonvolatile resistive random access memory (RRAM) device were observed.

Acknowledgements

The authors will acknowledge to Prof. Ting-Chang Chang and Prof. Cheng-Fu Yang. Additionally, this work will acknowledge the financial support of the National Science Council of the Republic of China (NSC 99-2221-E-272-003) and (NSC 100-2221-E-272-002).

Author details

Kai-Huang Chen[1], Chien-Min Cheng[2], Sean Wu[3], Chin-Hsiung Liao[4] and Jen-Hwan Tsai[4]

1 Department of Electronics Engineering/Tung-Fang Design University/Taiwan,R.O.C., Taiwan

2 Department of Electronic Engineering/Southern Taiwan University of Science and Technology/Taiwan, R.O.C., Taiwan

3 Department of Electronics Engineering/Tung-Fang Design University/Taiwan,R.O.C., Taiwan

4 Department of Mathematics and Physics/Chinese Air Force Academy/Taiwan, R.O.C., Taiwan

References

[1] Shannigrahi, R., & Jang, H. M. (2001). *Appl. Phys. Lett.*, 79, 1051.

[2] Hong, S. K., Suh, C. W., Lee, C. G., Lee, S. W., Hang, E. Y., & Kang, N. S. (2000). *Appl. Phys. Lett.*, 77-76.

[3] Xiong, S. B., & Sakai, S. (1999). *Appl. Phys. Lett.*, 75.

[4] Kim, J. S., & Yoon, S. G. (2000). *Vac. Soc. Technol.*, B, 18, 216.

[5] Wu, T. B., Wu, C. M., & Chen, M. L. (1996). *Appl. Phys. Lett.*, 69, 2659.

[6] Chen, K. H., Chen, Y. C., Yang, C. F., & Chang, T. C. (2008). *J. Phys. Chem. Solids*, 69, 461.

[7] Yang, C. F., Chen, K. H., Chen, Y. C., & Chang, T. C. (2007). *IEEE Trans. Ultrason. Ferroelectr. Freq. Control*, 54.

[8] Yang, C. F., Chen, K. H., Chen, Y. C., & Chang, T. C. (2008). *Appl. Phys. A-Mater. Sci. Process*, 90.

[9] Chen, K. H., Chen, Y. C., Chen, Z. S., Yang, C. F., & Chang, T. C. (2007). *Appl. Phys. A-Mater. Sci. Process*, 89, 533.

[10] Wu, S., Lin, Z. X., Lee, M. S., & Ro, R. (2007). *Appl. Phys. Lett.*, 102, 084908.

[11] Lee, S., Song, E. B., Kim, S., Seo, D. H., Seo, S., Won, K. T., & Wang, K. L. (2012). *Appl. Phys. Lett.*, 100, 023109.

[12] Yang, Y., Jin, L., & Yang, X. D. (2012). *Appl. Phys. Lett.*, 100, 031103.

[13] Scotta, J. F., Paz, C. A., & de Araujoa, B. M. (1994). *J. Alloys, Compounds*, 211 451.

[14] Araujo, C. A., Cuchiaro, J. D., Mc Millian, L. D., Scott, M. C., & Scott, J. F. (1995). *Nature (London)*, 374, 627.

[15] Park, B. H., Kang, B. S., Bu, S. D., Noh, T. W., Lee, J., & Jo, W. (1999). *Nature (London)*, 401, 682.

[16] Leu, C. C., Yao, L. R., Hsu, C. P., & Hu, C. T. (2010). *J. Electrochem. Soc.*, 157, 3, G85.

[17] Chen, K. H., Chen, Y. C., Yang, C. F., & Chang, T. C. (2008). *J. Phys. Chem. Solids*, 69.

[18] Yang, C. F., Chen, K. H., Chen, Y. C., & Chang, T. C. (2007). *IEEE Trans. Ultrason. Ferroelectr. Freq. Control*, 54 1726.

[19] Yang, C. F., Chen, K. H., Chen, Y. C., & Chang, T. C. (2008). *Appl. Phys. A*, 90 329.

[20] Chen, K. H., Chen, Y. C., Chen, Z. S., Yang, C. F., & Chang, T. C. (2007). *Appl. Phys. A*, 89 533.

[21] Watanabe, T., Funakubo, H., Osada, M., Noguchi, Y., & Miyayama, M. (2002). *Appl. Phys. Lett.*, 80 1.

[22] Kim, S. S., Song, T. K., Kim, J. K., & Kim, J. (2002). *J. Appl. Phys.*, 92 4.

[23] Noguchi, Y., & Miyayama, M. (2001). *Appl. Phys. Lett.*, 78 13.

[24] Velu, G., Legrand, C., Tharaud, O., Chapoton, A., Remiens, D., & Horowitz, G. (2001). *Appl. Phys. Lett.*, 79 659.

[25] Chen, K. H., Yang, C. F., Chang, C. H., & Lin, Y. J. (2009). *Jpn. J. Appl. Phys.*, 48 091401.

[26] Miao, J., Yuan, J., Wu, H., Yang, S. B., Xu, B., Cao, L. X., & Zhao, B. R. (2001). *Appl. Phys. Lett.*, 90 022903.

[27] Chen, K. H., Chen, Y. C., Chia, W. K., Chen, Z. S., Yang, C. F., & Chung, H. H. (2008). *Key Eng. Mater.*, 368-372.

[28] Wu, S. Y. (1974). *IEEE Trans. Electron Devices*, 21 499.

[29] Wu, S. Y. (1976). *Ferroelectrics*, 11 379.

[30] Sugibuchi, K., Kurogi, Y., & Endo, N. (1975). J. Appl. Phys. 46 2877. .

[31] Park, B. H., Kang, B. S., Bu, S. D., Noh, T. W., Lee, L., & Joe, W. (1999). *Nature (London)*, 401 682.

[32] Noguchi, Y., Miwa, I., Goshima, Y., & Miyayama, M. (2000). *Jpn. J. Appl. Phys*, 39 L1259.

[33] Noguchi, Y., & Miyayama, M. (2001). *Appl. Phys. Lett.*, 78 1903.

[34] Friessnegg, T., Aggarwal, S., Ramesh, R., Nielsen, B., Poindexter, E. H., & Keeble, D. J. (2000). *Appl. Phys. Lett.*, 77 127.

[35] Watanabe, T., Funakubo, H., Osada, M., Noguchi, Y., & Miyayama, M. (2002). *Appl. Phys. Lett.*, 80 1.

[36] Kim, S. S., Song, T. K., Kim, J. K., & Kim, J. (2002). *J. Appl. Phys.*, 92, 4.

[37] Noguchi, Y., & Miyayama, M. (2001). *Appl. Phys. Lett.*, 78 13.

[38] Rost, T. A., Lin, H., & Rabson, T. A. (1991). *Appl. Phys. Lett.*, 59 3654.

[39] Rost, T. A., Lin, H., Rabson, T. A., Baumann, R. C., & Callahan, D. C. (1991). IEEE Trans. Ultrason. Ferroelectr. Freq. Control, , 38

[40] Fleischer, S., Lai, P. T., & Cheng, Y. C. (1994). *J. Appl. Phys.*, 73 8353.

[41] Mihara, T., & Watanabe, H. (1995). *Part I, Jpn. J. Appl. Phys.*, 34 5664.

[42] Lin, Y. B., & Lee, J. Y. (2000). *J. Appl. Phys.*, 87 1841.

IntechOpen

IntechOpen